Measurement of Total Water with a Tunable Diode Laser Hygrometer: Inlet Analysis, Calibration Procedure, and Ice Water Content Determination

SEAN M. DAVIS, A. GANNET HALLAR,* AND LINNEA M. AVALLONE

Laboratory for Atmospheric and Space Physics, University of Colorado, Boulder, Colorado

WILLIAM ENGBLOM

Embry-Riddle Aeronautical University, Daytona Beach, Florida

(Manuscript received 5 December 2005, in final form 27 June 2006)

ABSTRACT

The University of Colorado closed-path tunable diode laser hygrometer (CLH), a new instrument for the in situ measurement of enhanced total water (eTW, the sum of water vapor and condensed water enhanced by a subisokinetic inlet), has recently been flown aboard the NASA DC-8 and WB-57F aircrafts. The CLH has the sensitivity necessary to quantify the ice water content (IWC) of extremely thin subvisual cirrus clouds (~0.1 mg m^{-3}), while still providing measurements over a large range of conditions typical of upper-tropospheric cirrus (up to 1 g m^{-3}). A key feature of the CLH is its subisokinetic inlet system, which is described in detail in this paper. The enhancement and evaporation of ice particles that results from the heated subisokinetic inlet is described both analytically and based on computational fluid dynamical simulations of the flow around the aircraft. Laboratory mixtures of water vapor with an accuracy of 2%–10% (2σ) were used to calibrate the CLH over a wide range of water vapor mixing ratios (~50–50 000 ppm) and pressures (~100–1000 mb). The water vapor retrieval algorithm, which is based on the CLH instrument properties as well as on the spectroscopic properties of the water absorption line, accurately fits the calibration data to within the uncertainty of the calibration mixtures and instrument signal-to-noise ratio. A method for calculating cirrus IWC from the CLH enhanced total water measurement is presented. In this method, the particle enhancement factor is determined from an independent particle size distribution measurement and the size-dependent CLH inlet efficiency. It is shown that despite the potentially large uncertainty in particle size measurements, the error introduced by this method adds ~5% error to the IWC calculation. IWC accuracy ranges from 20% at the largest IWC to 50% at small IWC (<5 mg m^{-3}).

1. Introduction

Cirrus clouds exert an influence on the earth's radiation budget that is disproportionate to their mass, due both to their location in the cold upper troposphere and to their unique optical and microphysical properties. Accurate knowledge of cirrus microphysical properties is essential to improving numerical weather predictions and general circulation climate models (e.g., Liou 1986). Furthermore, detailed microphysical information may lead to better small-scale models that focus on the processes inherent in cloud formation (i.e., nucleation and freezing; Houghton et al. 2001). In situ measurements of cirrus cloud microphysical properties are also needed to validate new satellite-based sensors and remote sensing techniques, as the near-global data from these sensors will be used to gain a more global picture of issues such as the water vapor budget in the Tropics and localized troposphere–stratosphere exchange.

One of the major challenges in measuring cirrus cloud microphysical properties is that they often span a range of several orders of magnitude. For example, previous measurements of cirrus cloud condensed water content range from $\sim 10^{-4}$ to 1 g m^{-3} (Dowling and Radke 1990). There have been relatively few direct measurements of cirrus cloud ice water content (IWC),

* Current affiliation: NASA Ames Research Center, Moffett Field, California.

Corresponding author address: Sean Davis, Laboratory for Atmospheric and Space Physics, University of Colorado, 1234 Innovation Dr., Boulder, CO 80303.
E-mail: seand@colorado.edu

DOI: 10.1175/JTECH1975.1

compared to those of other microphysical properties (Heymsfield and McFarquhar 2002). As a result, the representation of cloud radiative properties in global models relies on parameterizations created from a limited set of measurements or on derivations from related observations, such as determining IWC by integrating particle size distributions.

Several instruments exist for measuring the bulk density of the condensed phase of water in cirrus clouds, although it is important to note that most instruments, including the one described in this paper, do not measure ice water content directly. The Nevzerov probes (Korolev et al. 1998) directly measure liquid water content (LWC) or total water content (TWC) via the heat required to evaporate cloud droplets or particles impinging on a heated wire. IWC is determined by subtracting LWC from TWC. To date, the abilities of Nevzerov probes in cirrus clouds are not well established in the literature.

Other instruments for determining cirrus IWC operate on the principle of evaporating cloud hydrometeors and measuring the resultant humidity. These instruments can generally be classified by inlet type and method of measuring water vapor. The three established approaches to particle sampling in cirrus are the counterflow virtual impactor (CVI), isokinetic sampling, and subisokinetic sampling. Water vapor concentration is then determined by either Lyman-α photofragment fluorescence or tunable diode laser (TDL) spectroscopy. Each of these techniques has its advantages and limitations, which are briefly described below.

Twohy et al. (1997) describe a Lyman-α hygrometer coupled to a CVI for the measurement of condensed water content in both liquid and mixed-phase clouds. Recently, the Cloud and Precipitation Spectrometer and Imager (CSI) was developed by Twohy and colleagues. The CSI uses a TDL hygrometer coupled to a CVI similar to that described in Twohy et al. (1997). The CSI–CVI has the advantage of directly measuring the condensed phase of water (i.e., without the need for an independent water vapor measurement) with a fast time response. The main limitations of the CSI–CVI lie in the uncertainty related to the calculation of the particle enhancement factor, and bias due to the fraction of IWC below the particle cut size (minimum particle diameter collected with 50% efficiency), which is typically 10–20 μm, depending on airspeed and counterflow speed.

Both Harvard (HT; Weinstock et al. 2006) and the Met Office groups from the U.K. (UKMO; Brown 1993) have used a Lyman-α hygrometer to measure total water in an isokinetic system. The Harvard group subtracts water vapor measured simultaneously by the Harvard Lyman-α water vapor instrument (HW; Weinstock et al. 1994; Hintsa et al. 1999) to calculate condensed water content, whereas the Met Office group subtracts the saturation humidity with respect to ice at the ambient temperature and pressure.

In this paper, a new technique for the in situ measurement of enhanced total water (hereafter eTW) content in cirrus is presented. Enhanced total water is the sum of ambient water vapor and water vapor resulting from the evaporation of condensed water (liquid and/or ice) that has been enhanced above its ambient concentration by a subisokinetic inlet system. The instrument described herein was developed by modifying the open path, near-infrared TDL spectrometer commonly used for water vapor measurements (May 1998) into a closed-path system. When coupled with independent measurements of water vapor, aircraft speed, ambient pressure, and temperature, and (optionally) particle size distribution, the ice water content can be calculated.

In the following section, descriptions of the closed-path TDL hygrometer (CLH) and basic properties of the CLH measurement are presented. Then the sampling characteristics of the subisokinetic inlet system are described, including models for the particle sampling efficiency, heat transfer within the inlet, and ice crystal evaporation efficiency. In section 4 of this paper, laboratory calibrations and the CLH eTW retrieval algorithm are presented. In the final section, the ice water content determination is described and illustrated with an example of cirrus cloud data from the Midlatitude Cirrus Experiment (MidCiX).

2. Instrument design

The development of high-quality distributed-feedback TDLs specifically for water sensing began in 1992 at the Jet Propulsion Laboratory (JPL; May 1998). Single-frequency diode lasers are well suited for gas sensing because their line widths are usually of the order of a hundred megahertz, much narrower than the low pressure Doppler-broadened molecular line widths (e.g., May and Webster 1993). These lasers are also easily tunable with either current or temperature (or both) and often operate at room temperature, requiring only ~100 mW of power. Furthermore, these lasers are ideal for field missions because of their compact size and durability.

The TDL used in the University of Colorado CLH employs distributed feedback technology and was manufactured by the JPL Microdevices Laboratory. Specifically, the laser is composed of InGaAsP/InP, producing a midinfrared (7306.7518 cm^{-1} or ~1.37 μm)

source. The laser wavelength is tunable with either temperature or current; an increase of 1 mA in the injection current across the laser junction will tune the TDL wavelength by about 0.05 cm^{-1} (May 1998). In the CLH system, a thermoelectric element ("TE cooler") is used to keep the laser temperature fixed at approximately 15°C, and the laser wavelength is tuned by changing current. The IR detector, a standard InGaAs sensor (Sensors Unlimited, Princeton, NJ), is also mounted on a thermostated baseplate. The laser and detector are coupled to the absorption cell through small volumes capped with antireflection-coated quartz windows. Laser and detector housings are purged with ultra high purity nitrogen to minimize water vapor condensation in the optical volumes during flight.

The CLH has a closed, single-pass internal absorption cell that is 27.6 cm long. This cell consists of a 6-mm I.D. stainless steel tube sealed at both ends with antireflection-coated quartz windows. The pathlength limits the detection of water vapor to about 10 ppm for a 1-s integration. The temperature of the absorption cell is held fixed at 40°C (±0.01°C) with a custom pulse-width modulation (PWM) circuit coupled to a Minco thermofoil resistive heater. Control temperature and PWM parameters can be adjusted in the CLH instrument control software. Temperature is measured with a 30-kΩ thermistor. Pressure is measured at the midpoint of the absorption cell with a temperature-compensated solid-state gauge (Sensym model ASCX30AN, linearity ±0.1%) that is calibrated against a high-accuracy capacitance manometer (MKS Baratron 690A). Comparison to aircraft pressure shows no drift of the instrument pressure over time in flight.

The mass flow rate through the instrument is controlled by a mass flow controller (Tylan FC2901, Millipore, Inc.; with an accuracy of 0.1 std L min^{-1}) set at 1–2 std L min^{-1}, depending on flight conditions. Laboratory testing has verified that the flow controller performance does not change at flight pressures. The entire flow path is heated to 40° ± 1°C to evaporate ice crystals and water droplets, a process initiated by ram heating at the inlet (discussed further in section 3). Flow path heaters are Minco silicone rubber foil resistive elements, coupled to Minco CT325 controllers.

The laser control, signal processing, and data acquisition are accomplished with custom circuit boards in the PC104 format (MayComm, Inc., Pasadena, CA). The system operates under DOS running on an Ampro 100 MHz 486Dxi computer. Data are stored on a 96-MB disk-on-a-chip (MSystems, Inc.). A block diagram of the instrument is shown in Fig. 1, and the instrument dimensions, weight, and power requirements are shown in Table 1.

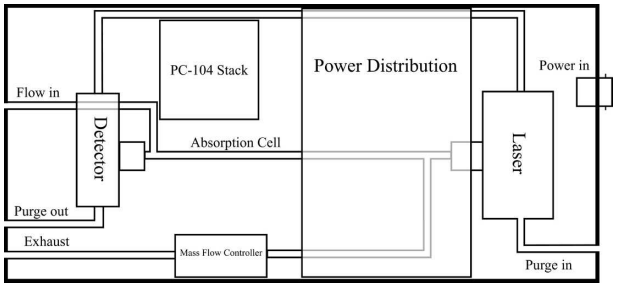

FIG. 1. A block diagram of the University of Colorado closed-path laser hygrometer.

The CLH uses second-harmonic absorption spectroscopy to measure water vapor resulting from the evaporation of cloud particles. Second-harmonic detection has been used with infrared TDLs to measure atmospheric trace gases with absorption coefficients as small as 10^{-7} (May and Webster 1993). For an in-depth description of the theory of second-harmonic absorption spectroscopy, see May and Webster (1993) or Webster et al. (1988). The CLH obtains both direct-absorption and second-harmonic ($2f$) spectra using the electronics package described by May (1998). Operating parameters are optimized to maximize the $2f$ amplitude and signal-to-noise ratio for measuring water vapor at pressures and concentrations typical of the upper troposphere and lower stratosphere (May and Webster 1993). Both direct-absorption and second-harmonic spectra are taken continuously during flight at about 8 Hz. In the current operational configuration, the two types of spectra are processed by computer software on the fly to generate four spectral parameters every 128 ms, while full spectra (512 points each), created by averaging 144 scans, are stored every 18 s. Examples of direct-absorption and second-harmonic spectra are shown in Fig. 2, along with the four key spectral parameters.

The four spectral parameters, which are used to retrieve the eTW value, are *power*, *powerzero*, *power*(v_0), and *pp2f* (see section 5). The *pp2f* is the peak-to-peak amplitude of the absorption feature in the second-harmonic spectrum. *Power*(v_0) is the value of the di-

TABLE 1. Instrument dimensions, weight, and power requirements.

Component	Dimensions (in.)	Weight (lb)	Power (W)
Water	20 × 10 × 6.5	21	15
Inlet	—	5.2	250*
Gas bottle**	10 × 6 × 6	8.2	N/A
Total	1660 $in.^3$	34.4	265

* Maximum value (all heaters full on).
** For purging optics includes regulator, fittings, and the pressure relief valve.

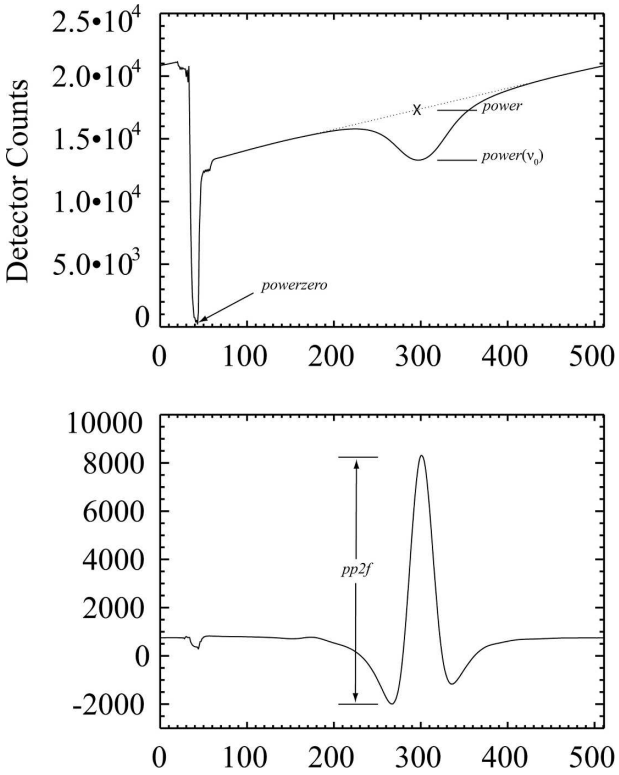

FIG. 2. Example of direct-absorption and second-harmonic spectra, with the four spectral parameters that are recorded at 8 Hz.

rect-absorption spectrum at maximum absorption. *Power* is defined as the average of two points a fixed distance in the scan before and after the location of *power*(v_0). To first order (i.e., as long as the sloping background in the direct-absorption spectrum is linear), *power* represents the detector signal if there were no absorption in the direct-absorption spectrum. *Powerzero* represents the background signal (detector dark counts) in the instrument and is recorded at the beginning of each scan, when the laser is momentarily turned off.

3. CLH inlet

The CLH originally flew aboard the National Aeronautics and Space Administration (NASA) DC-8 aircraft during the Third Stratopsheric Aerosol and Gas Experiment (SAGE III) Ozone Loss and Validation Experiment (SOLVE) field campaign based out of Kiruna, Sweden, in 1999/2000. More recently, the CLH has flown on the right wing pod of the NASA WB-57F aircraft during the Cirrus Regional Study of Tropical Anvils and Cirrus Layers-Florida Area Cirrus Experiment (CRYSTAL-FACE in 2002), MidCiX (in 2004), and Plume Ultrafast Measurements Acquisition (PUMA in 2004 and 2005) field campaigns. The CLH inlet described herein was used for CRYSTAL-FACE, MidCiX, and PUMA. A description of the inlet used for SOLVE is provided in Hallar et al. (2004).

The CLH is mounted behind a forward-facing, heated inlet located on the outboard side of the right-wing pod on the NASA WB-57F. The inlet is 0.65 m long with a 6-mm I.D., and consists of a carbon-fiber/epoxy composite tube surrounding a heated stainless steel inner tube. The space between these two concentric tubes is packed with Nomex insulation. The inlet tip is machined from Delrin, a thermally and electrically insulating plastic. Minco thermofoil resistive heaters are wrapped around the stainless steel inlet tube and placed in a special fixture near the inlet tip. The temperature of the heaters is set to 40°–50°C (±1°C) and is controlled by Minco CT325 temperature controllers with 30-kΩ feedback thermistors.

The CLH inlet was designed specifically for sampling thin cirrus with small condensed water amounts (<100 mg m^{-3}) by taking advantage of the inertial particle enhancement achieved in subisokinetic flow. In this scheme, particle concentrations are enhanced, relative to their ambient concentrations, in the CLH inlet when they have sufficient inertia such that they do not follow the streamlines around the inlet. In the most simplistic model of particle enhancement, large particles are enhanced by a factor of E over their ambient concentration, where $E = U/U_0$, U is the aircraft true airspeed, and U_0 is the instrument inlet speed. The E is commonly referred to as the inertial enhancement factor and represents the upper limit of particle enhancement that can be achieved with a subisokinetic inlet (neglecting particle reflections off surfaces around the inlet).

In reality, there are many factors that act to lower the particle enhancement in a subisokinetic inlet below the maximum inertial value. Divergent streamlines near the inlet tend to prevent the smallest particles from entering the inlet. In addition, the aircraft angle of attack α, which is defined here as the angle between the CLH inlet and the free-stream velocity vector, also acts to decrease the subtended volume (and hence the enhancement) by a factor of cosα.

For clarity, we shall define several terms used when discussing particle enhancement throughout the remainder of this paper. The particle enhancement factor EF is defined as the mass of particles per unit volume that enter the CLH absorption cell divided by the mass of all particles per unit volume in ambient air. Thus, the relationship between the eTW value (g m^{-3}) that is measured by the CLH, ambient water vapor concentration W (g m^{-3}), and ice water content IWC (g m^{-3}), is

$$\text{eTW} = \text{IWC} \times \text{EF} + W. \quad (1)$$

To obtain a value of EF that is more accurate than assuming EF = E, a particle size distribution (either canonical or as measured by a particle measurement probe) is combined with the so-called particle enhancement curve y. The particle enhancement curve is defined as the ratio of the number of particles per unit volume per unit size bin that enter the CLH inlet to the number of particles per unit volume per unit size bin in ambient air. The relationship between EF and y is

$$\mathrm{EF} = \frac{\int m(D)y(D)\,dD}{\int m(D)\,dD}, \tag{2}$$

where m is the mass distribution of particles with characteristic diameter D (mass of particles per unit volume per unit size).

An accurate prediction of particle enhancement requires characterization of both the particle distribution (e.g., density, size, shape) and the flow field in the vicinity of the inlet, which necessitates consideration of the inlet geometry (e.g., bluntness) and operating conditions (e.g., mass flow through the sensor) and also the influence of the aircraft itself on the local flow field. Analytical and semiempirical methods have been developed to study isoaxial, subisokinetic particle enhancement based on a Stokes flow assumption (Liu et al. 1989; Zhang and Liu 1989; Belyaev and Levin 1972; Vincent 1987). However, these approaches involve significant simplifying assumptions, especially regarding the nature of the local flow field. Consequently, we adopted the more rigorous particle tracking approach first described by Engblom and Ross (2003).

The Engblom–Ross methodology involves two steps. First, detailed, three-dimensional computational fluid dynamics (CFD) simulations are conducted to obtain a steady-state flow field for the WB-57F aircraft with the CLH inlet mounted in flight configuration on the right-wing pod. The inviscid (Euler) solution is calculated for a typical WB-57F flight condition from the CRYSTAL-FACE campaign. The CFD simulations were obtained using the general-purpose flow solver, GASP v4 (Aerosoft, Inc.), with an overlapping grid topology that included the WB-57F wing pod and CLH inlet/boom (see Fig. 3). The roughly 1-m-diameter wing pod has a significant influence on the flow field currents near the CLH inlet and, as a result, has a pronounced effect on particle enhancement.

The second step involves application of a 3D particle dynamics simulation (PDS) tool—a Lagrangian-type method—to track the trajectories of dense 2D sheets of evenly spaced spherical water-ice particles initialized upstream of the aircraft, as they would move relative to the aircraft in the vicinity of the inlet. Particles that are predicted to intercept the CLH inlet face are added to particle counts that are used to generate the particle enhancement curve. The inlet should receive a specific number of particle hits based on the areal density of particles within the initial sheet of particles (i.e., the free-stream areal density) and the inlet area (i.e., for a particle enhancement value of 1). The particles move through the CFD-generated flow field (and grid) toward the aircraft, restricted by a Courant-type time step restriction (i.e., particles are typically moved 10% of the distance between the nearest grid points per time step). The drag coefficient (C_D) is calculated at each time step along the trajectory using Eq. (3) (White 1991), which is valid for both Stokes flow and laminar flow over a sphere with accuracy of ±10%. Since we limit particle diameter to 1000 μm or less, the laminar flow assumption is valid for all flight conditions examined:

$$C_D = \frac{24}{\mathrm{Re}} + \frac{6}{1+\sqrt{\mathrm{Re}}} + 0.4, \quad 0 \le \mathrm{Re} \le 2 \times 10^5. \tag{3}$$

The predicted particle enhancement results from the CFD–PDS approach are provided in Fig. 4, along with curves calculated using the "blunt-inlet" model (Vincent 1987) and the "thin-walled" inlet model (Belyaev and Levin 1972). PDS results are shown for typical flight conditions of true airspeed (0.54 Mach), altitude (65 kft), and for two angles of attack (0° and 10°). The thin-wall result is a closer approximation to the presumably more accurate PDS results than the blunt-inlet

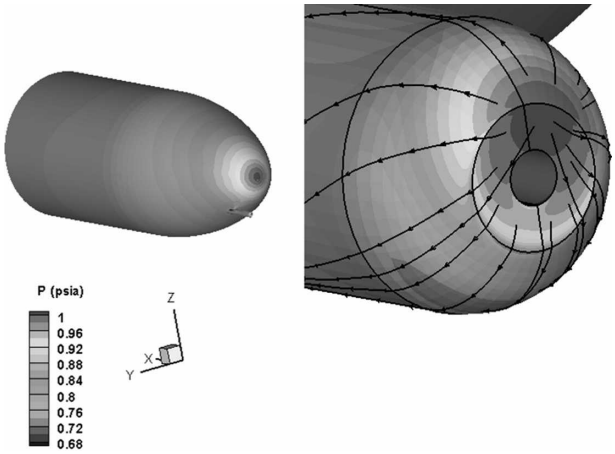

FIG. 3. (left) CFD-predicted surface pressure contours for WB-57F wing pod during level flight at 19.8 km (65 000 ft) with CLH instrument attached. (right) Close-up of the CLH inlet plus surface flow streamlines.

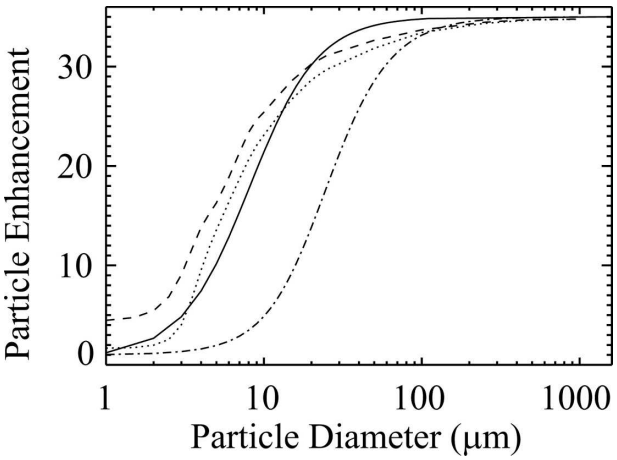

FIG. 4. The particle enhancement curve at nominal flight conditions ($U = 160$ m s^{-1}, $U_0 = 4.57$ m s^{-1}) calculated several different ways: the blunt-inlet (Vincent 1987; dash–dot) and thin-walled inlet (Belyaev and Levin 1972; solid) for reference, and CFD calculations specific to the WB-57F aircraft (dashed, $\alpha = 0°$; dotted, $\alpha = 10°$).

model. Increasing the wind pod angle of attack has an adverse effect on inlet efficiency, and this is apparently related to the increased effective bluntness of the wind pod, and resulting influence on the local flow field leading up to the inlet. The modest, sustained particle enhancement predicted by the PDS code for the smallest particles is related to the mass flow through the sensor. The larger the mass flow, the larger the portion of free-streamflow streamlines that will be influenced to reach the inlet. This positive influence in small particle enhancement is reduced significantly at the larger angle of attack. Although the PDS code predicts a modest level of particle enhancement due to assumed elastic particle reflection off nearby inlet surfaces, this effect is omitted from these results due to the tenuous nature of the elastic impact assumption. Since the CFD–PDS approach takes into account the specific geometry of the CLH inlet and WB-57F aircraft, these results are the most appropriate for use in the IWC calculations described in section 5.

Another issue that must be addressed is the extent to which particles evaporate before they reach the absorption cell. A Lagrangian model was used to track the evaporation of spherical ice particles of varying size as they traverse the CLH inlet. The model includes diffusion of water vapor from the surface of the sphere (i.e., sublimation) and the associated latent heat loss, thermal conduction of heat from the heated inlet air to the particle, and a time-dependent ice crystal temperature (which controls the evaporation/latent heating).

The governing equations for water vapor diffusion and heat transfer are

$$\frac{dm_d}{dt} = D_v 4\pi C_s F[\rho_v(\infty) - \rho_{\text{sat}}(T_p)], \tag{4}$$

$$\frac{dQ}{dt} = \rho_p V_p c_{\text{ice}} \frac{dT_p}{dt} = 4\pi C_s K F(T_{\text{inlet}} - T_p) + \ell \frac{dm_d}{dt} \tag{5}$$

(see, e.g., Mason 1971 or Heymsfield 1982), where m_d is the particle mass; D_v is the coefficient of water vapor diffusivity (m^2 s^{-1}); C_s is the shape factor (diameter/2 for spheres); F is the ventilation coefficient ($1 + 0.22 \times \text{Re}^{0.5}$ for spheres); $\rho_v(\infty)$ is the ambient water vapor density in the inlet; $\rho_{\text{sat}}(T_p)$ is the saturation vapor density at the surface of the crystal; ρ_p is the bulk density of solid ice (0.9 g cm^{-3}); V_p is the ice crystal volume; c_{ice} is the specific heat of ice; T_p and T_{inlet} are the temperatures of the particle and inlet, respectively; K is the thermal conductivity of air (W mK^{-1}); and ℓ is the latent heat of sublimation (vaporization) for particle temperatures less (greater) than 273.15 K.

For these calculations, the ambient water vapor density was varied linearly from a nominal value of 35 to 10 000 ppm over the length of the inlet to approximate the effect of an increase in humidity due to particle evaporation. These values roughly correspond to the water vapor mixing ratios at the endpoints of the CLH system (atmosphere and absorption cell). While 10 000 ppm is often an overestimate of eTW values measured by the CLH—which results in a slight overestimation of particle evaporation time—it is consistent with the highest values encountered during the field studies.

The results of the evaporation calculations are given in Fig. 5, which shows that solid ice spheres with diameters less than 30 μm are fully evaporated within the CLH inlet. This size roughly corresponds to solid columns (with $\rho_p = 0.91$ g cm^{-3} and length/width ratios of 4) of length 70 μm. Although the fully evaporated particle size may seem low considering the amount of condensed mass likely to exist at particle sizes greater than 30 μm, there are several additional considerations that affect the interpretation and applicability of the evaporation calculation. First, this model does not incorporate the full internal geometry of the flow system, which includes three 90° bends. As is shown in Fig. 5, particles larger than approximately 30 μm have a stopping distance greater than 6 mm, and thus impact the walls upstream of these bends, presumably shattering to smaller, and more easily evaporated, sizes. Moreover, cloud ice particles are frequently nonspherical and partially hollow at sizes greater than 30 μm, and ice crystal habit (and its corresponding effect on surface area) has a significant impact on particle evaporation times. For a particle with maximum dimension D, the evaporation

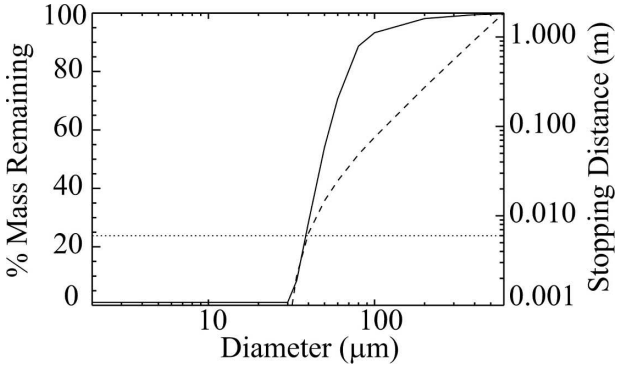

FIG. 5. The percent of ice crystal mass remaining (solid) after passing through the CLH inlet, and the stopping distance (dashed). The dotted line is at 6 mm, the diameter of the CLH inlet tubing. Particles with stopping distances greater than 6 mm impact the wall at the first 90° bend.

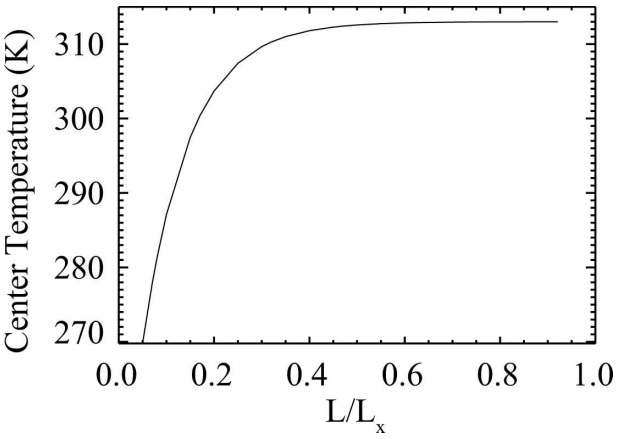

FIG. 6. The mean temperature at the center of the CLH inlet as a function of the nondimensional inlet length L/L_x, where L_x is the full length of the inlet system up to the absorption cell.

time for a spherical particle of diameter D represents the upper limit of possible evaporation times. Taken together, these factors mean that the calculation shown in Fig. 5 represent a lower limit to the fractional mass evaporated, and that particles that would not be fully evaporated impact the heated inlet wall, reducing their size and improving evaporation rates. Because of these complexities, the extent of particle evaporation in flight will be more fully explored in an instrument comparison paper based on observations made during the MidCiX and CRYSTAL-FACE campaigns.

Calculations were also performed to confirm that the mean temperature within the inlet and optical cell reached the heated temperature of the walls. Because flow within the CLH inlet is laminar (Reynolds number ~300), the approximation to the axial temperature profile from Sellars et al. (1956) is used. As can be seen in Fig. 6, the temperature at the radial center of the inlet develops rapidly with length toward the heated-wall value of 313 K.

4. CLH enhanced total water measurement

a. Enhanced total water retrieval algorithm

The algorithm for retrieval of the water vapor concentration in the CLH absorption cell (i.e., the enhanced total water) is based on the modeling of direct and second-harmonic spectra and the associated spectral parameters described in section 2. The technique for modeling second-harmonic spectra is similar to the procedure described by both May and Webster (1993) and May (1998). In our method, an array of mixing ratios and pressures expected in flight is used in conjunction with the H_2O line parameters from the high-resolution transmission molecular absorption (HITRAN) 2004 database (Rothman et al. 2005) to construct Voigt-profile transmission spectra in the range of a few wavenumbers around the H_2O line centered at 7306.752 cm^{-1}. These spectra include both self- and foreign broadening of the absorption line, as well as the effects of the finite laser line width.

The calculated spectra are then used to create synthetic direct and 2*f* spectra, from which the synthetic direct absorption, corresponding to 1 $power(\upsilon_0)/power$ in measured spectra, and 2*f* amplitude are derived. A surface plot of the synthetic *pp2f* shaded by synthetic direct absorption is shown in Fig. 7 as a function of pressure and mixing ratio.

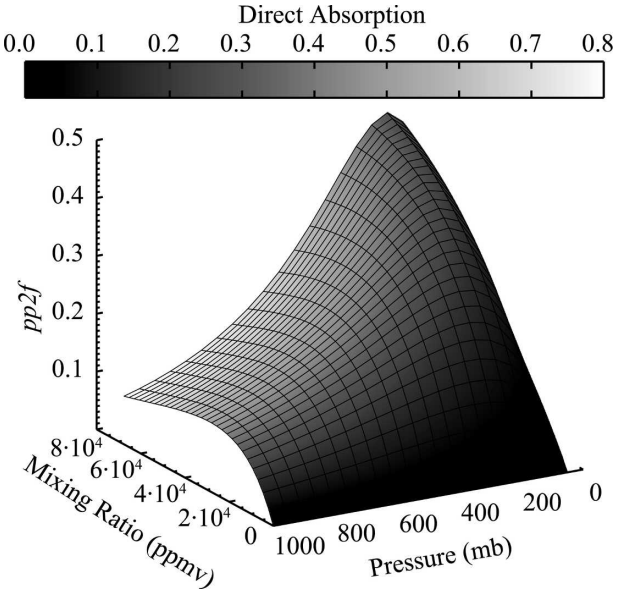

FIG. 7. A surface plot of the *pp2f* value vs water mixing ratio and absorption cell pressure, with the surface shaded according to the corresponding direct-absorption signal.

To create the synthetic *pp2f* and direct-absorption values shown in Fig. 7, one must know the laser modulation amplitude conversion Ω (cm^{-1} mA^{-1}) and the constant R_{cal} for conversion between detector signal and spectroscopic units, which is given by (following May and Webster 1993):

$$pp2f_{spectroscopic} = \frac{pp2f_{detector}}{R_{cal}\,(power\text{–}powerzero)}. \quad (6)$$

To obtain Ω and R_{cal}, we followed the method of May and Webster (1993) in which the laser injection current I is varied at a fixed pressure and water mixing ratio, and Ω and R_{cal} are determined from the fit of the measured *pp2f* values as a function of I.

For each measured data point, the measured pressure is used to create an array of direct-absorption and *pp2f* values for mixing ratios ranging from 1 to 70 000 ppm. The retrieved mixing ratio value is then the value in this array that gives the minimum "normalized" Euclidean distance (in direct-absorption/*pp2f* space) Δ, between the array and the measured direct absorption and *pp2f*, given by

$$\Delta = \sqrt{\left(\frac{pp2f_{synthetic} - pp2f_{measured}}{\sigma_{pp2f}}\right)^2 + \left(\frac{[power(\upsilon_0)/power]_{synthetic} - [power(\upsilon_0)/power]_{measured}}{\sigma_{dabs}}\right)^2}, \quad (7)$$

where σ_{pp2f} and σ_{dabs} are the precision of the *pp2f* and direct absorption, respectively. The precision is characterized in the laboratory by flowing water vapor mixtures through the instrument (described in section 4b) and computing the RMS deviation of the *pp2f* and direct-absorption values.

b. CLH calibrations

In principle, there is no need for laboratory calibrations of an instrument such as the CLH because the *2f* and direct-absorption spectra can be modeled and fit using the known H_2O line parameters and the instrument electronics response as described above. In practice, however, there are potential uncertainties and limitations to the approach described that warrant laboratory verification. For one, there may be limitations to the use of the four spectral parameters, which do not necessarily uniquely describe a spectrum, to determine the water vapor concentration. Elements related to instrument electronics, such as the nonlinear wavelength scale in the recorded spectra, are not modeled. Also, uncertainties in the H_2O absorption line strength [5%–10%, all error values from Rothman et al. (2005) and Toth (2005)], self-broadened width (5%–10%), air-broadened width (2%–5%), and temperature dependence of the air-broadened width (10%–20%) propagate into the synthetic direct-absorption and 2*f* amplitude in a manner that is difficult to quantify. For these reasons, it is necessary to perform laboratory calibrations to ensure that the water retrieval algorithm accurately captures the behavior that is measured.

Comprehensive calibrations of the CLH instrument were performed in 2003 at the National Center for Atmospheric Research (NCAR) Research Aviation Facility (RAF) and in 2005 at SpectraSensors, Inc. (more information available online at http://www.spectrasensors.com). These calibrations spanned mixing ratios of 50–55 000 ppm and pressures of 100–1000 mb, representing the range of conditions expected in the troposphere and lower stratosphere. Schematics of the two calibration setups are shown in Fig. 8.

In both sets of calibrations, the CLH measurements were compared to water vapor amounts created by Li-Cor Model 610 dewpoint generators, which can generate stable dewpoints from 0° to 50°C with an accuracy of ±0.2°C. Both dewpoint generators were calibrated by the National Institute of Standards and Technology (NIST). To monitor system stability and ensure that there were no leaks of ambient air that might influence the water amount in the calibration system, a chilled mirror hygrometer was included in both setups. For the 2003 calibrations, a General Eastern Hygrometer Model M4 was placed directly downstream of the dewpoint generator. The GE hygrometer measures dewpoints and frost points between −80° and +85°C with a chilled mirror sensor to within ±0.2°C. For the 2005 calibrations, an EdgeTech Dew Prime I chilled mirror hygrometer with a three-stage cooler was placed downstream of the CLH. The Dew Prime I measures dewpoints and frost points between −75° and +100°C with an accuracy of ±0.2°C.

To achieve water mixing ratios typical of flight conditions, it was necessary to dilute the output of the dewpoint generator. Mass flow controllers (MKS model 1359C, 1600 SCCM and/or model 1179, 10 SLPM for the 2003 calibrations; MKS model 1479 1 SLM and 20 SLM for the 2005 calibrations) were placed in series and in parallel with the dewpoint generator. Zero air (water content assayed by the supplier at less than 10 ppm) was used to dilute the dewpoint generator output to the level needed. For the larger mixing ratios (greater than 8000 ppm), no dilution was used. Pressure

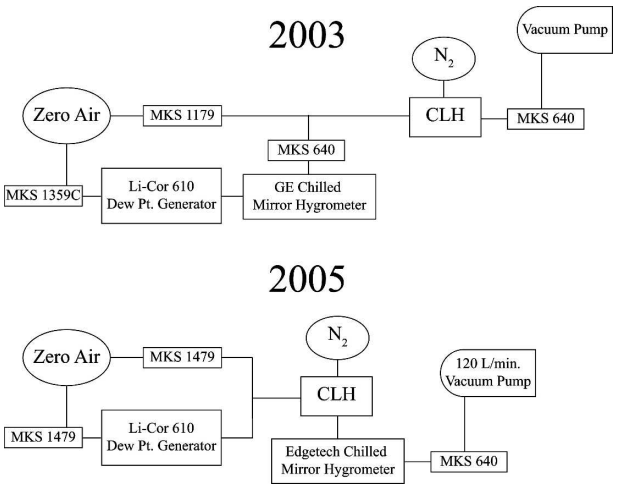

FIG. 8. Schematics of the CLH calibration setups.

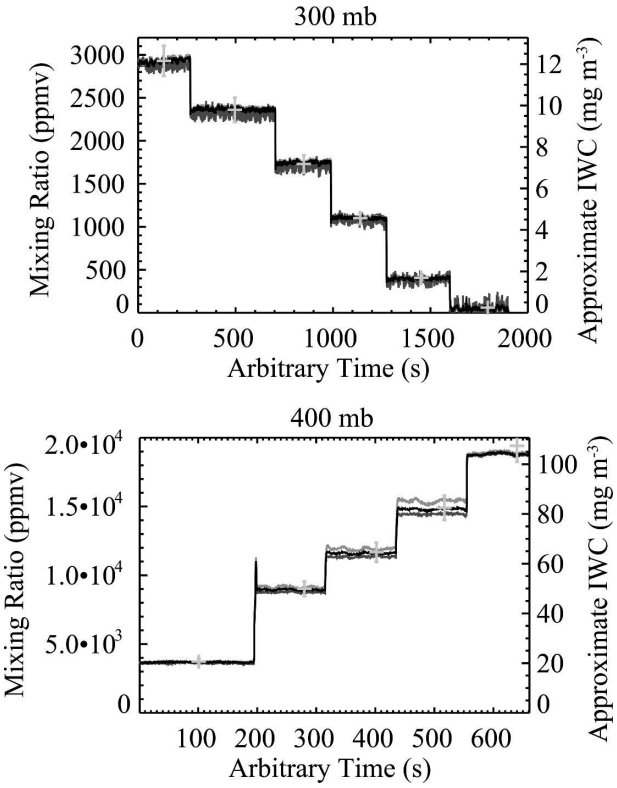

FIG. 9. Examples from the 2005 calibrations at (top) 300 and (bottom) 400 mb. The mixing ratio calculated three different ways is shown: using direct absorption (dark gray), *pp2f* (light gray), and combined using Eq. (7) (black). The calibration values (plus sign) and 2σ (6%) error bars are shown in the lightest gray.

was controlled in both calibration systems using an MKS 640 pressure controller downstream of the CLH. For the 2003 calibrations, additional pressure controllers were placed downstream of the dewpoint generator and frost point hygrometer to isolate the dewpoint generator and keep it near ambient pressure.

During the 2003 calibrations, a fixed mixing ratio of water vapor was generated and the pressure in the CLH absorption cell was varied in increments of about 100 mb over the range of 100–1000 mb. At each pressure step, the system was given adequate time to equilibrate, usually several minutes. Between runs with different mixing ratios, the equilibration time was usually much longer, up to an hour for the lowest mixing ratios. This equilibration time is a function of the water vapor mixture generation process, not the CLH response time. In Fig. 9, note the sharp transitions as water vapor amounts are changed. For the 2005 calibrations, the system pressure was varied in eight steps from 200 to 1060 mb with a fixed set point on the dewpoint generator. At each pressure, the water vapor mixing ratio was varied, using the mass flow controllers, over a range from about 100 to 50 000 ppm (dependent on pressure). An example of the calibration data from 2005 is shown in Fig. 9. In this figure, values of both the calibration water vapor mixing ratio and the corresponding approximate IWC are shown. Approximate IWC (mg m^{-3}) is calculated by conversion of Eq. (1) to density units using EF = 50 and WV = 0, to illustrate the correspondence between laboratory mixing ratio values and IWC values encountered in flight. The top panel shows a run of low mixing ratios at 300 mb, and the bottom panel shows a run of high mixing ratios at 400 mb. In both panels, the water vapor concentration calculated three different ways [*pp2f* only, direct absorption only, and combined via Eq. (7)] is shown.

For the 2003 calibrations, the uncertainty in the mixtures created for the CLH calibration is the result of uncertainties associated with each component of the calibration system. The mixing ratio (q) for each calibration mixture is given by

$$q = \frac{f_1}{f_1 + f_2} \frac{p_{\text{sat}}(T_d)}{p_{\text{ambient}}} \times 10^{-6}, \tag{8}$$

where f_1 is the mass flow rate through the dewpoint generator, f_2 is the dilution mass flow rate, $p_{\text{sat}}(T_d)$ is the saturation vapor pressure of the air at the dewpoint measured by the GE hygrometer, and p_{ambient} is the air pressure at the GE hygrometer. The uncertainty associated with each of these components is given in Table 2. Propagating the error from these values using Eq. (8), the uncertainty of the mixing ratio of the mixtures created for the 2003 calibrations is 2%–10% (2σ), depending on the values of T_d and the flow rates f_1 and f_2.

For the 2005 calibrations, the uncertainty in the water vapor mixtures is about 6% (2σ) and arises primar-

TABLE 2. The 2003 calibration uncertainties.

Mass flow controller No. 1	0.5%
Mass flow controller No. 2	1%
Ambient pressure	0.5% of reading
T_d	±0.2°C
Total uncertainty (2σ)	2%–10%

ily from uncertainties in the dewpoint and pressure measurements, assuming that the mixtures are well mixed and no leaks are present in the system between the CLH and EdgeTech hygrometer.

c. *Accuracy of CLH enhanced total water measurement*

The accuracy of the CLH water vapor measurement is constrained by several factors, including the accuracy of the mixtures used in calibration, the accuracy of the model that produces synthetic spectra, and the accuracy of the interpolation scheme used to look up mixing ratio from measured *pp2f*, direct absorption, and pressure. Ideally, the accuracy of the CLH eTW measurement is the same as that of the CLH laboratory water vapor measurement, because the absorption cell operating conditions (specifically pressure/temperature) are the same in the laboratory and in flight. In reality, biases in the eTW measurement may be introduced by hysteresis, purge air impurities, and continuous desorption of water vapor from the inlet walls. Purged air impurities and continuous desorption of water from walls would cause an offset in the clear-air value relative to the water vapor amount. An example of how these effects can be corrected is shown in Hallar et al. (2004). Hysteresis, and the effect of these issues on the IWC calculation, are further explored in Davis et al. (2006, manuscript submitted to *J. Geophys. Res.*). For the remainder of this paper, it is assumed that these issues are negligible, or can be corrected, and thus do not contribute to uncertainty in the CLH eTW measurement.

To assess the accuracy of the eTW measurement, water vapor mixing ratio calculated with the retrieval algorithm is compared to the mixing ratio of the calibration mixture calculated by Eq. (8) (2003 calibrations) or measured by the frost point hygrometer (2005 calibrations). This approach sidesteps the need to evaluate and combine the contributions from individual uncertainties, instead evaluating the overall agreement between the eTW retrieval and the calibration value. Figure 10 illustrates the results of this comparison by plotting as a histogram the percentage error of the water value obtained from the retrieval compared to the calibration value. Because the standard deviation of the errors shown in Fig. 10 is of the order of the 10% (2σ) uncertainty quoted for the calibration mixtures, the uncertainties associated with the retrieval algorithm and other factors listed above are negligible, and the accuracy of the CLH enhanced total water measurement is of the order of the accuracy of the water vapor mixtures used in calibration.

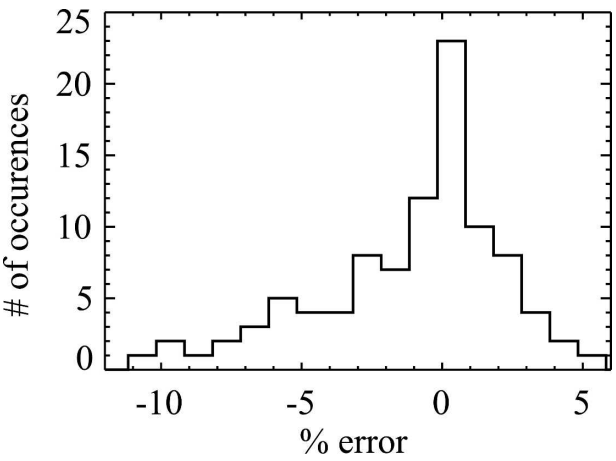

FIG. 10. A histogram of the percentage error of the water values resulting from the retrieval algorithm compared to the known calibration value.

5. Ice water content determination

The determination of cirrus cloud IWC using the CLH eTW measurement involves data from multiple instruments aboard the WB-57F aircraft, as well as knowledge of the airflow around the CLH inlet from the CFD–PDS calculations in section 3. A schematic of the process of calculating IWC is shown in Fig. 11 and will serve as a useful reference in the following description.

First, the contribution from water vapor must be subtracted from the eTW measurement. On the WB-57F, there are typically two water vapor instruments, the JPL Laser Hygrometer (JLH; May 1998) and the Harvard water vapor instrument (Weinstock et al. 1994). Because of differences in calibration and instrument performance, the instruments (CLH, JLH, HT, and HW) do not always report the same values in clear air. As illustrated in Hallar et al. (2004), the clear-air differences between the CLH and water vapor measurements are small compared to typical in-cloud eTW values, and can be corrected for using baseline fits to the offset in clear-air data.

Next, data quality is checked. For the CLH, the *pp2f* value can be corrupted by the improper identification of the 2*f* peak by the instrument software. While this

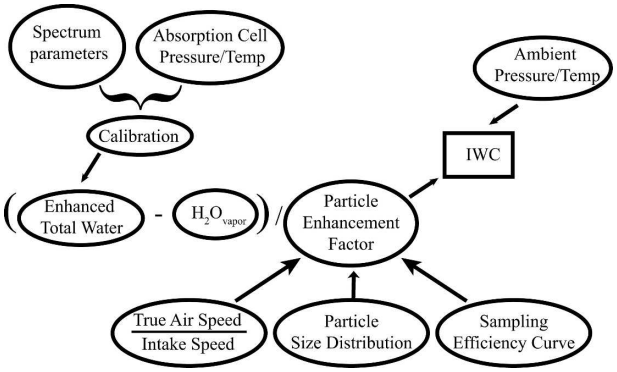

FIG. 11. A schematic showing the process for calculating IWC.

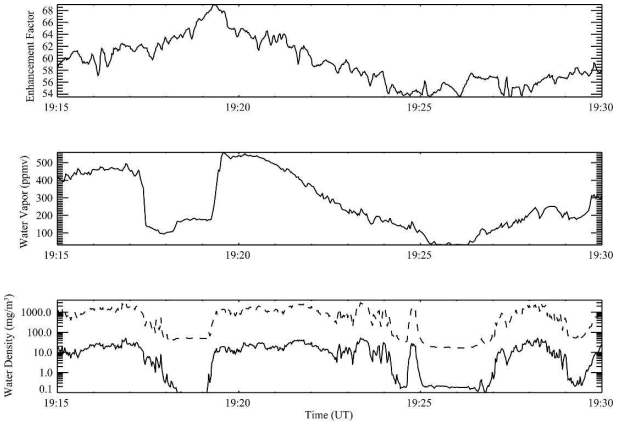

FIG. 12. (top) Enhancement factor, (middle) water vapor mixing ratio, and (bottom) enhanced total water (dashed line) and IWC (solid line) from the 2 May 2004 flight during the MidCiX campaign.

rarely happens, it is usually when the TE cooler on the laser is struggling, often during descent into a very warm, moist air mass. Data at cruise altitudes are unaffected. For the water vapor measurements, suspect data points that are flagged in the publicly available data files on the NASA Earth Science Project Office (ESPO) Web archive (see online at http://espoarchive.nasa.gov/archive/index.html) are removed. The water vapor data are interpolated to the times of the CLH measurement and subtracted.

Next, the particle enhancement factor is calculated. When particle size distribution (PSD) measurements are not available, the inertial enhancement factor ($E = U_0/U$) is used. When PSD measurements are available, they are used.

To calculate EF from PSD measurements, the particle enhancement curve is calculated from the aircraft true airspeed (TAS), CLH inlet intake speed, and aircraft angle of attack. TAS and angle of attack are measured with an accuracy of ± 1 m s^{-1} and $\pm 0.03°$, respectively, by the Meteorological Measurement System (MMS) instrument suite mounted in the nose of the WB-57F (Scott et al. 1990). The CLH intake speed is calculated from the mass flow rate through the instrument, inlet temperature, and ambient (static) pressure, also measured by the MMS. The next step is to integrate the particle enhancement curve with a particle size distribution as described in Eq. (2). For CRYSTAL-FACE and MidCiX, data from the Cloud, Aerosol, and Precipitation Spectrometer (CAPS; Baumgardner 2002) were used because they report the largest range of particle sizes (1–1600 μm). Typically, particle size data are aggregated over 10-s intervals to minimize errors from counting statistics. The aggregated data are then interpolated back onto the time base of the CLH data for integration to produce the final particle enhancement factor (EF). An example of the EF, eTW, IWC, and Harvard water vapor is shown in Fig. 12 for a short segment of the 2 May 2004 MidCiX flight to illustrate the components of the IWC calculation.

Finally, the IWC in units of density (mg m^{-3}) is calculated from Eq. (1), and IWC in units of mixing ratio can be calculated using the ambient pressure and temperature (from the MMS system),

$$\mathrm{IWC(ppm)} = \frac{\mathrm{IWC(mg\ m^{-3})}RT_{\mathrm{static}}}{Mp_{\mathrm{static}}} 1 \times 10^6, \quad (9)$$

where M is the molecular mass of water and R is the universal gas constant.

Uncertainty in ice water content calculation

The accuracy of the IWC calculation derives from uncertainties in all of the components described in the previous section; specifically, IWC uncertainty is a result of the individual uncertainties in the eTW measurement, water vapor measurement, particle EF, and extent of particle evaporation. Because of the limitations of the particle evaporation modeling in section 3, the extent of particle evaporation within the CLH inlet is assessed using flight data in Davis et al. (2006, manuscript submitted to *J. Geophys. Res.*). In this section, we ignore any potential particle evaporation issues, and quantify the accuracy due to the other factors involved in the IWC calculation.

The uncertainty for the CLH eTW measurement is 10% (2σ), and the particle enhancement curve uncertainty is estimated to be 5%, due to particle reflection and interpolation uncertainty. The uncertainty for the JLH water vapor measurement is 10% at pressures typical of CRYSTAL-FACE and MidCiX (May 1998). The MMS true airspeed accuracy is ± 1 m s^{-1} (Scott et al. 1990) and the CLH flow speed uncertainty is 7.5%–

10%. From the above values, it is possible to calculate the CLH IWC uncertainty by propagating errors through Eq. (1) under the assumption that there is no size dependence to the sampling efficiency (i.e., EF = $E = U/U_0$). This simplified approach allows for an estimation of the IWC uncertainty without quantifying the complex errors associated with particle size measurements and CFD calculations. The resulting uncertainty under this assumption depends on the specific values of eTW and water vapor, but ranges from 20% to 50% (2σ) for IWC less than 5 mg m^{-3} and asymptotes to about 22% (2σ) for IWC values greater than 5 mg m^{-3}.

By calculating the EF using E instead of Eq. (2), EF is systematically overestimated, and a dry bias is introduced into the IWC value. To assess the significance of this dry bias, we evaluate flight data from MidCiX. In this dataset, the mean and median dry bias are 10% and 7%, respectively. It should be noted that any systematic uncertainties in the CAPS data could affect these values, but they are only intended as a rough estimate of the level of bias that would be introduced by calculating IWC from the CLH eTW measurements in the absence of a particle size measurement.

In addition to removing the IWC dry bias, the use of Eq. (2) for EF adds uncertainty to the IWC calculation. To assess the contribution to IWC uncertainty from EF calculated using Eq. (2), it is necessary to estimate the contributions from both the measured particle size distribution and calculated particle enhancement curve. In general, particle size measurement errors are not well constrained, but the CAPS uncertainty in number concentration is estimated to be 15%–25%, and particle sizing uncertainty is estimated at 20% (D. Baumgardner 2006, personal communication). Because of the complex nature of error propagation from these variables into the final EF, their contribution was calculated using a Monte Carlo simulation and CAPS data from MidCiX. In this simulation, random (Gaussian) error was introduced into the CAPS number concentration and size based on uncertainties quoted above. Also, random error ranging from 50% at the smallest sizes to 5% at the largest sizes (based on the bounds of the two CFD curves in Fig. 4) was introduced into the particle enhancement curve. Including these additional sources of error adds an additional 5% to the total IWC error given above. The large uncertainties in particle size distributions do not affect the IWC measurement much because most of the mass in these distributions is at particle sizes where the CLH sampling efficiency is close to unity.

Although there is no absolute standard that can be used to verify the accuracy of IWC measurements in flight, comparison with several independent measurements of IWC can give confidence in the accuracy of all instruments (e.g., Davis et al. 2006, manuscript submitted to *J. Geophys. Res.*)

6. Conclusions

In this paper, the University of Colorado closed-path laser hygrometer instrument properties, calibration, enhanced total water measurement, and IWC calculation have been described. The CLH measures enhanced total water over the range of pressures and mixing ratios found in the troposphere and lower stratosphere with an accuracy of about 10% (2σ).

The CLH inlet is specifically designed to create inertial enhancement of particles in thin cirrus clouds, and under nominal flight conditions enhances ice particles by a factor of about 50 over their ambient concentrations. Detailed CFD calculations show that particles about 5 μm in diameter are enhanced by about 50% of the inertial enhancement factor, and that the EF increases with particle size, reaching an asymptotic value of the inertial enhancement factor at sizes between 70 and 100 μm. Calculations of evaporation for spherical ice crystals were performed, and reveal that the maximum particle diameter that is fully evaporated within the CLH inlet is at least 30 μm. The geometry of the inlet, however, promotes shattering of large crystals, so it is likely that the maximum size evaporated is significantly larger.

The CLH has been calibrated with two different calibration systems over a large range of mixing ratios and pressures. The algorithm for retrieving enhanced total water uses the spectroscopic properties of the water vapor molecule, CLH laser modulation settings, and detector properties to calculate synthetic direct-absorption and second-harmonic spectra over a wide range of mixing ratios and pressures. The measured values of direct and second-harmonic absorption are then compared to these synthetic values at a given pressure to determine the mixing ratio. Using calibration data, this algorithm is shown to be accurate to 10% (2σ), close to the level of uncertainty associated with the calibration mixtures themselves.

In addition to the enhanced total water algorithm, a method for calculating the cirrus cloud IWC is presented that uses meteorological, water vapor, and particle size data from other instruments aboard the NASA WB-57F aircraft. Given estimates for the uncertainty in the particle size data, it is estimated that the uncertainty in the cirrus IWC measurement is about 27% (2σ), with larger uncertainties (approaching 50%) for very small IWC values (<5 mg m^{-3}), as a result of the small differences between the enhanced total water

and water vapor values. It is estimated that a dry bias of the order of 10% is introduced if one calculates the IWC in the absence of particle size data, based on measurements at midlatitudes.

Acknowledgments. We thank Teresa Campos and Randy May for making their facilities available to us for calibrations, and for providing advice throughout the calibration process. We acknowledge numerous helpful conversations with Andy Heymsfield about particle evaporation. Funding for the calibration and data analysis described herein was provided to L. M. Avallone by NASA's Radiation Sciences Program, under the direction of Don Anderson and Hal Maring. We appreciate the help of the WB-57F flight and ground crews, and the work of Stephen Lane and Roger Gunderson who designed and fabricated the CLH inlet.

REFERENCES

Baumgardner, D., H. Jonsson, W. Dawson, D. O'Connor, and R. Newton, 2002: The cloud, aerosol and precipitation spectrometer (CAPS): A new instrument for cloud investigations. *Atmos. Res.,* **59–60,** 251–264.

Belyaev, S. P., and L. M. Levin, 1972: Investigation of aerosol aspiration by photographing particle tracks under flash illumination. *Aerosol Sci.,* **3,** 127–140.

Brown, P. R. A., 1993: Measurements of ice water content in cirrus using an evaporative technique. *J. Atmos. Oceanic Technol.,* **10,** 579–590.

Dowling, D. R., and L. F. Radke, 1990: A summary of the physical properties of cirrus clouds. *J. Appl. Meteor.,* **29,** 970–978.

Engblom, W., and M. Ross, 2003: Numerical model of airflow induced particle enhancement for instruments carried by the WB-57F aircraft. ATR-2004(5084)-1, The Aerospace Corporation, El Segundo, CA, 23 pp.

Hallar, A. G., L. M. Avallone, R. L. Herman, B. E. Anderson, and A. J. Heymsfield, 2004: Measurements of ice water content in tropopause region Arctic cirrus during the SAGE III Ozone Loss and Validation Experiment (SOLVE). *J. Geophys. Res.,* **109,** D17203, doi:10.1029/2003JD004348.

Heymsfield, A. J., 1982: A comparative study of the rates of development of potential graupel and hail embryos in high plains storms. *J. Atmos. Sci.,* **39,** 2867–2897.

——, and G. M. McFarquhar, 2002: Mid-latitude and tropical cirrus: Microphysical properties. *Cirrus,* D. K. Lynch et al., Eds., Oxford University Press, 78–101.

Hintsa, E. J., E. M. Weinstock, J. G. Anderson, R. D. May, and D. F. Hurst, 1999: On the accuracy of *in situ* water vapor measurements in the troposphere and lower stratosphere with the Harvard Lyman-α hygrometer. *J. Geophys. Res.,* **104,** 8183–8189.

Houghton, J. T., Y. Ding, D. J. Griggs, M. Noguer, P. J. van der Linden, X. Dai, K. Maskell, and C. A. Johnson, Eds., 2001: *Climate Change 2001: The Scientific Basis.* Cambridge University Press, 881 pp.

Korolev, A. V., J. W. Strapp, G. A. Isaac, and A. N. Nevzorov, 1998: The Nevzorov airborne hot-wire LWC–TWC probe: Principle of operation and performance characteristics. *J. Atmos. Oceanic Technol.,* **15,** 1495–1510.

Liou, K. N., 1986: Influence of cirrus clouds on weather and climate processes: A global perspective. *Mon. Wea. Rev.,* **114,** 1167–1199.

Liu, B. Y. H., Z. Q. Zhang, and T. H. Kuehn, 1989: A numerical study of inertial errors in anisokinetic sampling. *J. Aerosol Sci.,* **20,** 367–380.

Mason, B. J., 1971: *The Physics of Clouds*. 2d ed. Oxford University Press, 671 pp.

May, R. D., 1998: Open-path, near-infrared tunable diode laser spectrometer for atmospheric measurements of H_2O. *J. Geophys. Res.,* **103,** 19 161–19 172.

——, and C. R. Webster, 1993: Data processing and calibration for tunable diode laser harmonic absorption spectrometers. *J. Quant. Spectrosc. Radiat. Transfer,* **49,** 335–347.

Rothman, L. S., and Coauthors, 2005: The HITRAN 2004 molecular spectroscopic database. *J. Quant. Spectrosc. Radiat. Transfer,* **96,** 139–204.

Scott, S. G., T. P. Bui, K. R. Chan, and S. W. Bowen, 1990: The meteorological measurement system on the NASA ER-2 aircraft. *J. Atmos. Oceanic Technol.,* **7,** 525–540.

Sellars, J. R., M. Tribus, and J. S. Klein, 1956: Heat transfer to laminar flow in a round tube or flat conduit: The Graetz problem extended. *Trans. ASME,* **78,** 441–448.

Toth, R. A., 2005: Measurements and positions, strengths, and self-broadened widths of H_2O from 2900 to 8000 cm^{-1}: Line strength analysis of the 2nd triad bands. *J. Quant. Spectrosc. Radiat. Transfer,* **94,** 51–107.

Twohy, C. H., A. J. Schanot, and W. A. Cooper, 1997: Measurement of condensed water content in liquid and ice clouds using an airborne counterflow virtual impactor. *J. Atmos. Oceanic Technol.,* **14,** 197–202.

Vincent, J. H., 1987: Recent advances in aspiration theory for thin walled and blunt aerosol sampling probes. *J. Aerosol Sci.,* **18,** 487–498.

Webster, C. R., R. T. Menzies, and E. D. Hinkley, 1988: Infrared laser absorption: Theory and applications. *Laser Remote Chemical Analysis,* R. M. Measures, Ed., John Wiley, 163–272.

Weinstock, E. M., and Coauthors, 1994: New fast response photofragment fluorescence hygrometer for use on the NASA ER-2 and the Perseus remotely piloted aircraft. *Rev. Sci. Instrum.,* **65,** 3544–3554.

——, and Coauthors, 2006: Measurements of the total water content of cirrus clouds. Part I: Instrument details and calibration. *J. Atmos. Oceanic Technol.,* **23,** 1397–1409.

White, F. M., 1991: *Viscous Fluid Flow*. 2d ed. McGraw-Hill, Inc., 614 pp.

Zhang, Z. Q., and B. Y. H. Liu, 1989: On the empirical fitting equations for aspiration coefficients for thin walled sampling probes. *J. Aerosol Sci.,* **20,** 713–720.